PHYSICAL REVIEW APPLIED **19,** 064085 (2023)

Generation of Spin-Wave Pulses by Inverse Design

S. Casulleras,[1,2,*] S. Knauer,[3] Q. Wang,[3] O. Romero-Isart,[1,2] A.V. Chumak,[3] and
C. Gonzalez-Ballestero[1,2,†]

[1] *Institute for Quantum Optics and Quantum Information of the Austrian Academy of Sciences, Innsbruck 6020, Austria*
[2] *Institute for Theoretical Physics, University of Innsbruck, Innsbruck 6020, Austria*
[3] *Faculty of Physics, University of Vienna, Vienna 1090, Austria*

(Received 23 November 2022; revised 16 April 2023; accepted 2 June 2023; published 30 June 2023)

The development of fast magnonic information-processing devices requires operating with short spin-wave pulses, but, the shorter the pulses, the more affected they are by information loss due to broadening and dispersion. The capability of engineering spin-wave pulses and controlling their propagation could solve this problem. Here, we provide a method to generate linear spin-wave pulses with a desired spatial-temporal profile in magnonic waveguides based on inverse design. As relevant examples, we theoretically predict that both rectangular and self-compressing spin-wave pulses can be generated in state-of-the-art waveguides with fidelities $\gtrsim 96\%$ using narrow stripline antennas. The method requires minimal computational overhead and is universal, i.e., it applies to arbitrary targeted pulse shapes, type of waves (exchange or dipolar), waveguide materials, and waveguide geometries. It can also be extended to more complex magnonic structures. Our results could lead to the utilization of large-scale magnonic circuits for classical and quantum information processing.

DOI: 10.1103/PhysRevApplied.19.064085

I. INTRODUCTION

Spin waves, exhibiting strong nonlinearity and low-loss coefficients, are promising candidates for classical and quantum information processing [1–3] and surpass their electric current-based counterpart by harnessing properties such as frequency and phase [4–8]. The demonstrations of coherent spin-wave transport in nanoscale magnetic structures and prototype devices [9–13] allow access to the further miniaturization of large-scale magnonic circuits. Most of these works focus on tailoring spin-wave propagation through spatial-temporal nanostructure engineering [10,11,14,15] or by coupling to other systems, such as paramagnetic spins [16–19] or acoustic waves [20,21]. Recently, the concept of inverse design has been introduced into magnonics numerically [15,22] and experimentally [23], and has shown its great potential for radiofrequency applications as well as for Boolean and neuromorphic computing. In these investigations, a medium through which a spin wave propagates was designed to obtain the required functionality, while the wave itself was excited continuously. However, modern high-performance computing demands the use of short pulses that carry data at high clock rates. The fact that spin-wave dispersions are not linear and the different spectral components of the pulse have different group velocities leads to a broadening and distortion of the pulse shape, resulting in data loss. The minimum duration of the pulse is also limited by the bandwidth of the spin-wave spectrum.

Here we propose an inverse design method (IDM) to obtain linear spin-wave pulses of arbitrary target shape at any point of a waveguide. The method is universal, i.e., it is suitable for both dipolar or exchange spin waves and for waveguides made of any material and with any geometry. As examples, we theoretically demonstrate the generation of self-compressing and rectangular pulses in state-of-the-art yttrium-iron-garnet (YIG) nanowaveguides. The self-compressing pulses possess an increased amplitude in a defined local point of a waveguide, enabling addressed read and write of data or local triggering of nonlinear phenomena in classical and quantum magnonic networks. The rectangular-wave pulses are of great interest for radiofrequency and binary data processing as they allow the highest (undisturbed) data-transmission rate. It is shown that the IDM provides a pulse-generation fidelity close to unity.

This paper is organized as follows. First, we provide a stepwise method for the determination of the voltage signal, which must be applied to a narrow but arbitrarily shaped antenna to generate an arbitrary target spin-wave pulse, using minimal micromagnetic simulations. Then,

---

[*] silvia.casulleras-guardia@uibk.ac.at
[†] carlos.gonzalez-ballestero@uibk.ac.at

we illustrate our method for three particular examples in state-of-the-art YIG nanowaveguides [9,24,25], namely the generation of a self-compressing spin-wave pulse and a rectangular pulse, both in the exchange regime, and of a self-compressing spin-wave pulse in the dipolar regime. Our results are verified by micromagnetic simulations using MuMax3 [26]. Additionally, we discuss both the pulse-generation fidelity and the energy cost for pulse generation as a function of antenna size. Finally, a discussion of our results is presented in the Conclusion.

II. METHOD FOR INVERSE DESIGN OF SPIN-WAVE PULSES

Pulse engineering comprises the generation of tailored wave packets able to evolve into a desired shape after propagation within a given nanostructure. It provides a method to control wave propagation without nanostructure engineering. Pulse engineering is used to control optical excitations [27–29], acoustic waves [30], or microwaves [31] for applications such as quantum information processing [32–35]. Pulse engineering could thus bring to magnonic devices capabilities of interest for classical and quantum technology. Here, we propose a method for spin-wave pulse engineering based on inverse design, i.e., a method to determine the magnetic driving needed to generate a chosen target pulse.

To model spin-wave pulse engineering, we focus on the experimentally relevant system shown in Fig. 1(a), namely an infinite single-band magnonic waveguide with arbitrary cross section, oriented along the x axis and driven by a microwave antenna of width w_a centered at $x = x_a$. This antenna models experimental configurations where spin waves are excited by narrow striplines coupled to impedance-matched waveguides [36–38], hence providing high voltage-to-spin-wave transmission efficiencies. The antenna generates a magnetic field $\mathbf{B}_1(\mathbf{r}, t) = \mathbf{B}_a(\mathbf{r})V(t)$, with a spatial profile $\mathbf{B}_a(\mathbf{r})$ given by the antenna geometry and a dimensionless driving $V(t)$ proportional to the applied voltage [39]. The magnetic field $\mathbf{B}_1(\mathbf{r}, t)$ generates spin waves, i.e., a propagating dynamic magnetization $\mathbf{m}(\mathbf{r}, t)$ on top of the stationary waveguide magnetization. The purpose of the IDM is to determine the driving $V(t)$ needed to generate a spin-wave pulse whose magnetization, at a chosen time t_f, transverse position (y_0, z_0), and waveguide arm $x > x_a$, has a chosen target pulse shape $m_T(x)$, that is, $\mathbf{e}_0 \cdot \mathbf{m}(x, y_0, z_0, t_f) \propto m_T(x)$, where $\mathbf{e}_0$ is an arbitrary unit vector.

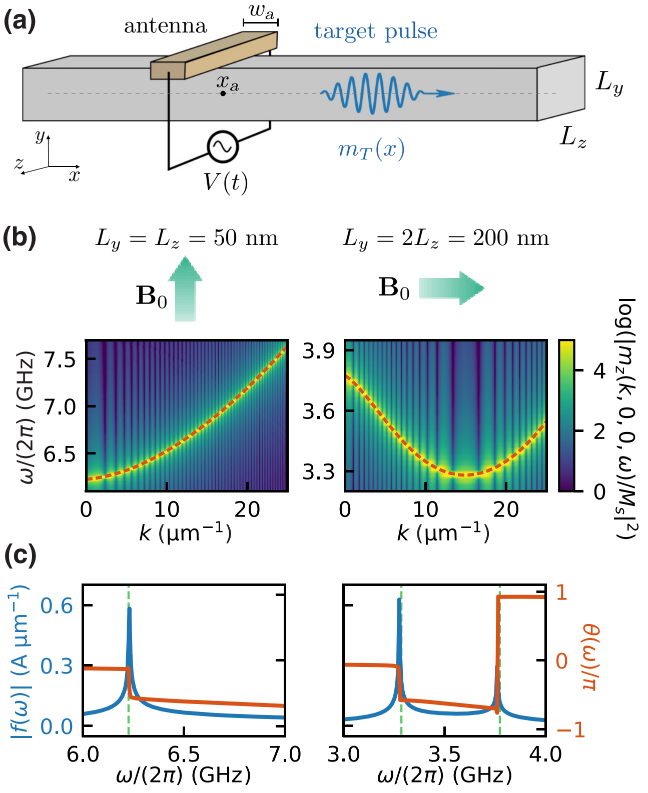

FIG. 1. System charaterization. (a) Schematic of the generation of a target spin-wave pulse in a single-band waveguide of arbitrary cross section. Our IDM provides the antenna driving $V(t)$ needed to generate a pulse with a given shape $m_T(x)$ along the waveguide axis using a microwave antenna of width w_a centered at $x = x_a$. (b) Examples of dispersion relations for YIG waveguides with a rectangular cross section of 50×50 nm^2 and a transverse bias field (left) and a rectangular cross section of 100×200 nm^2 and a longitudinal bias field (right). (c) Modulus (blue) and phase (orange) of the waveguide transfer function (definition in the main text) at $\mathbf{r} = \mathbf{0}$ for the same two waveguide configurations, for antenna widths $w_a = 70$ nm (left) and $w_a = 230$ nm (right). Here and in the remaining figures we fix $x_a = 0$. The dashed lines mark the cutoff frequencies at which $d\omega/dk = 0$. See Appendix A for details on the simulations.

The IDM consists of three steps (see Appendices A and B for details): (i) The characterization of the system by calculating the waveguide static magnetization, its dispersion relation $\omega(k)$, and the antenna transfer function $\mathbf{f}(\mathbf{r}, \omega)$. The transfer function is defined in the frequency domain as the relation between the driving applied to the antenna and the magnetization generated by it at position $\mathbf{r}$, i.e., $\mathbf{m}(\mathbf{r}, \omega) \equiv \mathbf{f}(\mathbf{r}, \omega)V(\omega)$. Each of these quantities can be calculated efficiently with simple micromagnetic simulations. (ii) The calculation of the *time-dependent* magnetization $\mathbf{m}_T(x_a, y_0, z_0, t)$, at the chosen transverse position (y_0, z_0) and at the antenna longitudinal position $x = x_a$, which would evolve into the target pulse after free propagation in the waveguide. This magnetization is computed by evolving the pulse *backward* in time while recording the magnetization at $\mathbf{r} = (x_a, y_0, z_0)$. The backward evolution is performed until the whole pulse lies at the other side of the antenna ($x < x_a$), a time which we set as $t = 0$. We use the following approximate expression for the time evolution, valid in the linear regime and for low propagation losses:

$$\mathbf{m}_T(\mathbf{r},t) \simeq \frac{1}{\sqrt{2\pi}} \int_{\mathbb{R}} dk \left(\mathbf{c}(k;y,z) e^{i(kx-\omega(k)t)} + \text{c.c.} \right), \quad (1)$$

where the coefficients $\mathbf{c}(k;y,z)$ are determined by the constraint $\mathbf{e}_0 \cdot \mathbf{m}(x,y_0,z_0,t_f) = m_T(x)$. (iii) The computation of the required driving as $V(t) = \mathcal{F}^{-1}\{\mathcal{F}\{\mathbf{e}_0 \cdot \mathbf{m}_T(x_a,y_0,z_0,t)\}/[\mathbf{e}_0 \cdot \mathbf{f}(x_a,y_0,z_0,\omega)]\}$, where $\mathcal{F}$ and $\mathcal{F}^{-1}$ denote the Fourier and inverse Fourier transforms, respectively.

This IDM is valid for any dispersion relation and any target shape not forbidden by physical constraints (e.g., too wide antennas, see example below). It thus provides a universal recipe for the generation of spin-wave pulses in the linear regime. The method is also computationally efficient as steps (ii) and (iii) do not require additional micromagnetic simulations. An essential advantage of this IDM is the use of the approximate expression Eq. (1), which allows to backward evolve the pulse with minimal computational overhead.

III. RELEVANT EXAMPLES: SELF-COMPRESSING AND RECTANGULAR PULSES

We demonstrate the performance and universality of our IDM by theoretically studying the generation of pulses relevant for magnonic information processing, and benchmarking it against full micromagnetic simulations. Specifically, we consider the generation of two classes of pulses, namely self-compressing and rectangular pulses, in different waveguides showing different spin-wave regimes (exchange and dipolar). Self-compressing pulses are a family of chirped pulses that compress as they propagate along the waveguide due to the curvature of the dispersion relation [40]. At the time of maximum compression, these pulses have a Gaussian intensity profile whose spot size can be subwavelength. In contrast to related ideas, such as nonlinear spin-wave bullets or solitons [41–44], these self-compressing pulses remain within the linear regime, and thus require less power and exhibit less dissipation due to magnon-magnon scattering. In magnonics, self-compressing pulses could be used to enhance the interaction between propagating spin waves and local elements (e.g., magnetic islands [45] or resonators [46]), or to partially compensate for propagation losses by compressing all the intensity at the position of the detector, thereby enabling the detection of otherwise too weak signals. The subwavelength compression can also allow quantum nodes to be locally addressed within an ensemble of densely packed nodes, an idea that has been explored in the context of microwave photonic quantum information processing [40,47]. Furthermore, although in this work we focus on the linear regime, the compression of one or several pulses at the same point in space can create a strong and localized nonlinear response, a feature that could be used as a synapse trigger in magnon-based neuromorphic computing [48,49]. As a second example we consider the generation of rectangular pulses, which are the basis of digital information processing as they maximize bit rate and information readability.

A. Self-compressing pulse in the exchange regime

First, we focus on the generation of a self-compressing pulse in the exchange regime. We consider a YIG nanowaveguide with a square cross section of 50 nm width and a transverse bias field, which has been used in recent experiments [24]. The dispersion relation and transfer function of this waveguide are shown in Figs. 1(b) and 1(c) (left panel). We use the following Gaussian target pulse [40],

$$m_T(x) = A \exp\left(-\frac{\left(x - x_f\right)^2}{4\sigma_f^2} \right) \cos\left(k_0 x\right), \quad (2)$$

where A is the amplitude of the pulse (chosen to ensure that nonlinearity is negligible), k_0 is its carrier wave number, x_f the point of maximum compression, and σ_f the width at $x = x_f$. The self-compressing behavior of this pulse is evident in its backward time evolution, shown in Fig. 2(a) (left panel). For the parameters used in the figure, the initial pulse width (i.e., standard deviation of intensity, see Appendix C for details), $\sigma(0) = 5.27$ μm, shrinks to a final value $\sigma(t_f) \approx \sqrt{2}\sigma_f = 295$ nm at $t = t_f$ (horizontal dashed line), thus reaching subwavelength spin-wave compression ($\sigma(t_f)k_0/(2\pi) < 1$). To generate this pulse using our IDM we consider a narrow antenna of width $w_a = 70$ nm, in order to efficiently excite all the pulse wave numbers k [see Fig. 2(b)]. Using the backward time evolution [Fig. 2(a)] and the transfer function of this antenna [Fig. 1(c)] we obtain the driving $V(t)$ needed to generate the pulse, shown in frequency domain in Fig. 2(c). We then test our result by applying the obtained driving to the antenna and calculating the exact magnetization dynamics using a full micromagnetic simulation (see Appendix A for details). The resulting generated magnetization profile, which we label $\mathbf{m}_g(\mathbf{r},t)$, is shown in Fig. 2(a) (right panel). Note that, although we focus on the right arm of the waveguide ($x > 0$), identical pulses are generated at both sides of the antenna as the system is mirror symmetric around $x = x_a = 0$. At $x = x_f$ the pulse has a duration of 2.81 ns (defined as the temporal variance, see Appendix C for details). The target and generated pulses at $t = t_f$ (both square normalized) are shown in Fig. 2(d). To quantify the performance of our method we define the pulse-generation

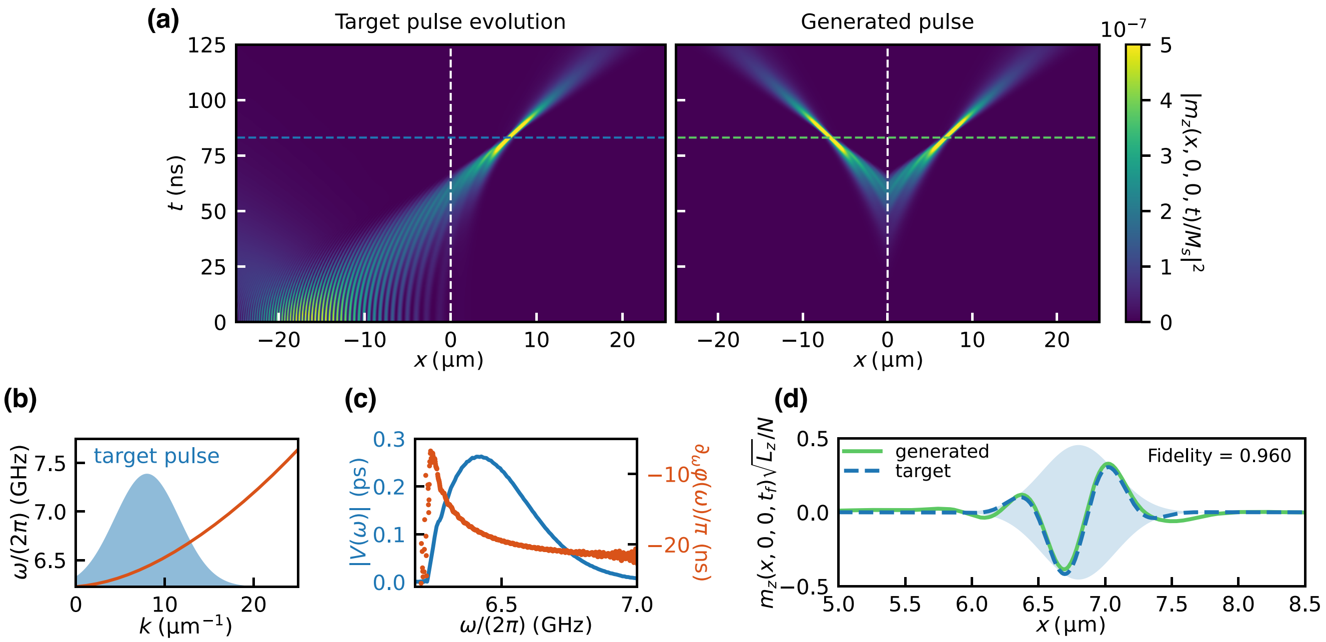

FIG. 2. Generation of a self-compressing spin-wave pulse in the exchange regime. (a) Magnetization as a function of position along the waveguide and time. Left: Backward evolution of the target pulse Eq. (2) in a square YIG waveguide of $L_y = L_z = 50$ nm width under a transverse bias field $\mathbf{B}_0 = (270\text{ mT})\mathbf{e}_y$. The pulse parameters are $x_f = 6.8\mu$m, $\sigma_f = 194$ nm, $k_0 = 8\ \mu\text{m}^{-1}$ and $A/M_s = 0.004$, where M_s is the saturation magnetization. Right: micromagnetic simulation of the magnetization dynamics under the antenna driving $V(t)$ obtained with our IDM, with chosen parameters $t_f = 83$ ns, $x_a = y_0 = z_0 = 0$, and $\mathbf{e}_0 = \mathbf{e}_z$. In both panels, horizontal and vertical lines indicate t_f and the antenna position $x_a = 0$, respectively. (b) Polynomial fit of the waveguide dispersion relation (orange) and envelope of the target pulse Eq. (2) in reciprocal space (shaded area). (c) Modulus (blue) and derivative of the argument (orange) of the frequency-domain driving function $V(\omega) = |V(\omega)|e^{i\varphi(\omega)}$ extracted from our IDM. (d), Comparison between the target magnetization (dashed blue line) and the magnetization generated at $t = t_f$ by applying our IDM according to micromagnetic simulations (solid green line). Both magnetizations are square normalized using $N^2 \equiv \int_{\mathbb{R}} dx(\mathbf{e}_0 \cdot \mathbf{m}(x, y_0, z_0, t_f))^2$. The shaded area shows the envelope of the target pulse.

fidelity as

$$F(t) \equiv \frac{\left[\int_0^\infty dx\, m_g(x,t) m_T(x)\right]^2}{\int_0^\infty dx\, m_g^2(x,t) \int_0^\infty dx\, m_T^2(x)}, \tag{3}$$

where $m_g(x,t) \equiv \mathbf{e}_0 \cdot \mathbf{m}_g(x, y_0, z_0, t)$. For the chosen parameters a maximum fidelity $F = 0.963$ is achieved at $t = 83.07$ ns $\approx t_f$, certifying the success of our generation method. We attribute the small approximately equal to 4% errors to frequency-dependent propagation losses not considered in Eq. (1).

B. Rectangular pulse in the exchange regime

As a second example we focus on the generation of a rectangular pulse in the exchange regime. We consider the same system as above, namely a 50×50 nm^2 square YIG waveguide excited by an antenna with $w_a = 70$ nm. We use the following rectangular target pulse:

$$m_T(x) = \frac{A}{2}\left[\operatorname{erf}(x_+) + \operatorname{erf}(x_-)\right]\cos(k_0 x), \tag{4}$$

where $x_\pm \equiv (\Delta x \pm 2(x - x_f))/(2\sqrt{2}\sigma_c)$ and $\operatorname{erf}(x)$ is the error function. Here, k_0 is the carrier wave number, A the amplitude, x_f the center of the pulse, Δx its spatial extension, and σ_c determines the curvature at the edge of the rectangular envelope. The generation of this pulse using the driving $V(t)$ obtained by our IDM is shown in Fig. 3(a). Similarly to the self-compressing pulses, the amplitude $|V(\omega)|$ [shown in Fig. 3(c)] closely resembles the shape of the target pulse in reciprocal space, which is given by a sinc function [Fig. 3(b)]. For these parameters the pulse-generation fidelity is $F = 0.979$ [Fig. 3(d)], demonstrating the successful pulse generation. The pulse duration at $x = x_f$ is 1.96 ns.

C. Self-compressing pulse in the dipolar regime

As a third example, in Fig. 4(a) we demonstrate the generation of a self-compressing pulse in the dipolar (backward-volume) wave regime of a YIG waveguide with a rectangular cross section of 200×100 nm^2. In this configuration, the derivative of the dispersion is negative in the range $|k| \lesssim 15\ \mu\text{m}^{-1}$ [see right panel of Fig. 1(b)]. The target pulse is thus chosen within this wave-number

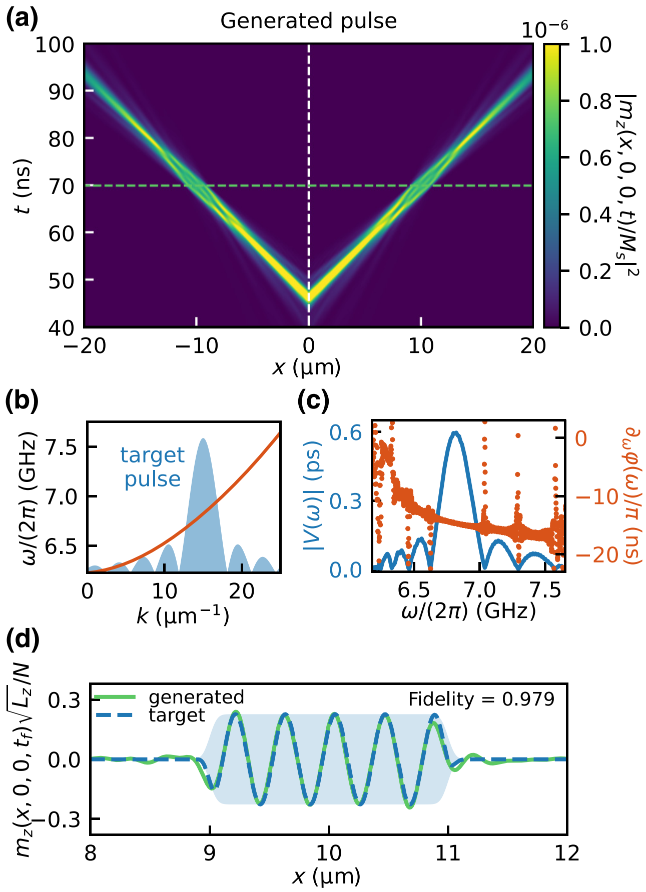

FIG. 3. Generation of a rectangular spin-wave pulse in the exchange regime. (a) Micromagnetic simulation of the magnetization dynamics in a square YIG waveguide of $L_y = L_z = 50$ nm width, under a transverse bias field $\mathbf{B}_0 = (270\ \mathrm{mT})\mathbf{e}_y$ and under the antenna driving $V(t)$ given by our IDM. We choose an antenna width $w_a = 70$ nm, the target pulse Eq. (4), and parameters $k_0 = 15\ \mu\mathrm{m}^{-1}$, $x_f = 10\ \mu\mathrm{m}$, $\Delta x = 2\ \mu\mathrm{m}$, $A/M_s = 0.004$, $\sigma_c = 0.05\ \mu\mathrm{m}$, $t_f = 70$ ns, $x_a = y_0 = z_0 = 0$, and $\mathbf{e}_0 = \mathbf{e}_z$. (b) Polynomial fit of the dispersion relation (orange) and envelope of the target pulse in reciprocal space (shaded area). (c) Extracted modulus (blue) and derivative of the argument (orange) of the required driving function $V(\omega) = |V(\omega)|e^{i\varphi(\omega)}$ in frequency domain. (d) Target magnetization (dashed blue line, envelope shown by shaded area) and magnetization generated by our IDM at $t = t_f$ extracted from the micromagnetic simulation (solid green line). Both magnetizations are square normalized.

range [see Fig. 4(b)] and leftward propagating along the opposite waveguide arm $x < x_a$. Moreover, for this waveguide the dispersion relation is degenerate in the range 3.30 GHz $\lesssim \omega/(2\pi) \lesssim$ 3.75 GHz, i.e., there are two spin-wave modes with the same energy and different wave numbers. To guarantee that the spin-wave pulse is only generated in the region of negative derivative of the dispersion we choose a larger antenna ($w_a = 230$ nm), which is unable to excite wave numbers larger than approximately

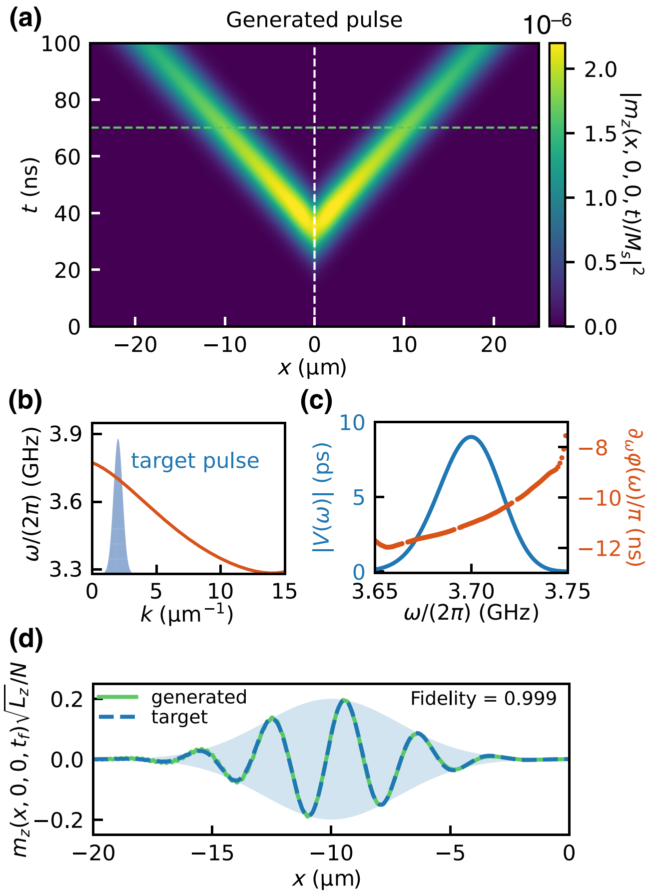

FIG. 4. Generation of a self-compressing pulse in the dipolar regime. (a) Micromagnetic simulation of the magnetization dynamics in a YIG rectangular waveguide of $200 \times 100\ \mathrm{nm}^2$ cross section under a longitudinal bias field $\mathbf{B}_0 = (50\ \mathrm{mT})\mathbf{e}_x$ and the antenna driving $V(t)$ given by our IDM. We choose an antenna width $w_a = 230$ nm and parameters $x_f = -10\ \mu\mathrm{m}$, $\sigma_f = 2\ \mu\mathrm{m}$, $k_0 = 2\ \mu\mathrm{m}^{-1}$, $A/M_s = 0.004$, $t_f = 70$ ns, $x_a = y_0 = z_0 = 0$, and $\mathbf{e}_0 = \mathbf{e}_z$. (b) Polynomial fit to the dispersion relation of the waveguide (orange) and target pulse envelope in reciprocal space (shaded area). (c) Extracted modulus (blue) and derivative of the phase (orange) of the required driving function $V(\omega) = |V(\omega)|e^{i\varphi(\omega)}$ in frequency domain. (d) Target magnetization (dashed blue, envelope shown by shaded area) and magnetization generated at $t = t_f$ extracted from the micromagnetic simulation (solid green). Both magnetizations are square normalized.

$\pi/w_a = 13.6\ \mu\mathrm{m}^{-1}$. The resulting pulse generation has a fidelity of $F = 0.999$, as shown in Fig. 4(d).

D. Dependence on antenna size

Although the narrow antennas used in Figs. 2 and 3 are experimentally feasible, wider antennas are, in practice, desirable as they are simpler to fabricate and provide higher spin-wave excitation efficiency. In Fig. 5(a) we study the pulse-generation fidelity as a function of antenna width w_a, for the three example pulses shown above.

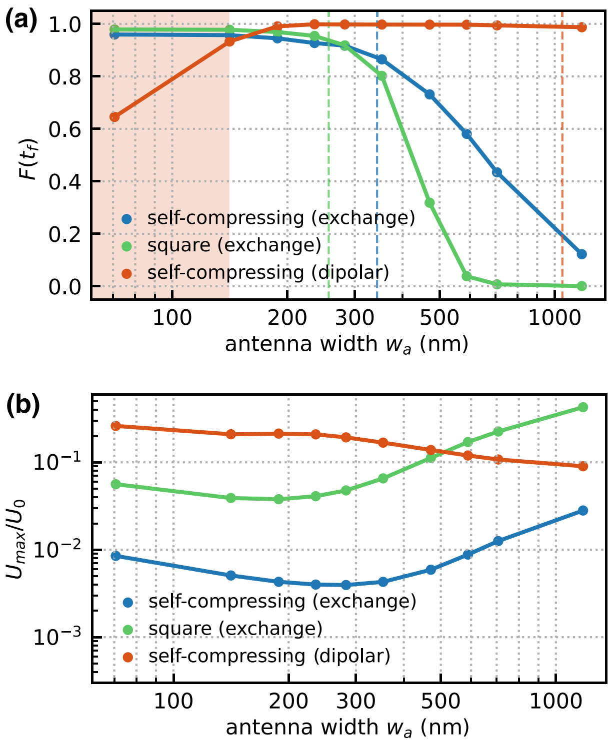

FIG. 5. Pulse generation using wide antennas. (a) Pulse generation fidelity as a function of antenna width w_a for the three pulses shown in Figs. 2–4. For each antenna width the pulse has been rescaled so that its peak amplitude remains constant. The dashed vertical lines indicate the minimum wavelengths $\lambda_{\min}$ of each pulse ($\lambda_{\min}/2$ for the dipolar-regime pulse). The shaded area indicates the region where the fidelity for the dipolar-regime pulse decreases below 0.9 due to the excitation of degenerate modes. (b) Maximum value $U_{\max}$ of the instantaneous magnetic energy of the driving magnetic field as a function of antenna width w_a, normalized to the energy associated to the homogeneous field $\mathbf{B}_0$ used in each case. See Appendices C and D for the definitions of minimum wavelength and energy. In both panels, solid lines are a guide to the eye.

As an antenna cannot generate spin waves with wavelengths smaller than approximately $2w_a$, the generation fidelities are bound to decrease for $w_a \gtrsim \lambda_{\min}$, with $\lambda_{\min}$ the minimum wavelength of the pulse (see Appendix C for a definition). Generation fidelities above 90% can still be achieved at $w_a \lesssim 300$ nm for the pulses of Figs. 2 and 3, and beyond $w_a = 1$ μm for the spatially much wider backward-volume pulse of Fig. 4. For the latter, the decrease in fidelity for narrow antennas, indicated by the shaded area, stems from the excitation of unwanted, high-wave-number modes in the degenerate dispersion relation [Fig. 1(b), right panel]. Within the regions of high fidelity, the energy required to generate the pulse is reduced for wider antennas. This is indicated in Fig. 5(b) where, as a figure of merit for energy cost, we display the maximum value of the instantaneous energy stored in the waveguide by the antenna driving field (see details in Appendix D).

We emphasize that the low-fidelity regions in Fig. 5(a) do not manifest a failure of our method but an unphysical choice of the target pulses, which cannot be generated by antennas of certain widths.

The different classes of pulses considered in this work show that the IDM method enables near-perfect generation of spin-wave pulses of arbitrary shape in both the exchange and the dipolar regime. The IDM method can be directly applied to single-band structures with arbitrary geometry (e.g., waveguides, films), provided that the voltage-to-spin-wave transmission efficiency of the antenna is sufficiently high. Moreover, one can show that the specific shape of the antenna does not affect the performance of the method, provided that its width is smaller than the minimum pulse wavelength, $w_a \lesssim \lambda_{\min}$. Finally, since the IDM relies on micromagnetic simulations to characterize the structure, it can be applied to more complex systems with, e.g., arbitrary pinning boundary conditions, Dzyaloshinskii-Moriya interactions, etc. Thus, our IDM provides a universal method for spin-wave pulse engineering.

IV. CONCLUSION

We propose a method for universal spin-wave pulse engineering based on inverse design. The method provides, in a numerically efficient way, the time-dependent driving which can be applied to a narrow antenna to generate an arbitrary target spin-wave pulse in the linear regime. Our concept is universal as it applies to arbitrary waveguide and antenna geometries, and to both the exchange and dipolar regimes. Using micromagnetic simulations, we theoretically show high-fidelity generation of relevant pulses for magnonics. Specifically, we predict the generation of a self-compressing pulse both in the dipolar and the exchange regime with fidelities $F > 0.95$. Moreover, we predict the generation of rectangular pulses of duration $\sigma_t = 1.96$ ns with fidelity $F = 0.98$. In the 50×50 nm^2 waveguide modeled in this work, and with antennas of width $w_a = 70$ nm, our method allows generation of pulses as short as $\sigma_t \approx 2\pi[\omega(\pi/w_a) - \omega(0)]^{-1} = 0.26$ ns, thus allowing for fast magnon-based information processsing. Even shorter pulse durations could be attained in materials with higher exchange stiffness constant such as Ga:YIG (e.g., Refs. [50,51]). In addition, the presented inverse design method can be extended to other magnonic structures, and could be refined at the cost of higher computational complexity, e.g., by including wavelength-dependent spin-wave losses in the backward propagation step.

Our results pave the way for implementing various nanophotonics-inspired strategies, and particularly inverse design, in magnon-based technology. Coherent magnon pulse generation and control is needed for future implementations of photonics-inspired quantum gates: square pulses with specific durations are needed to perform single-qubit gates (e.g., π pulses, arbitrary rotations) on localized qubits, such as superconducting qubits laterally coupled to a magnonic waveguide. In addition, the self-compressing pulses shown in this work could be used to perform nonlinear operations on propagating magnonic qubits "on the fly" with high speed and low decoherence. Indeed, these pulses would self-activate the needed nonlinearity only at the compression spot while keeping the propagation linear (i.e., less affected by decoherence) elsewhere. Moreover, due to the short wavelengths of spin waves, incorporating magnonic devices into microwave photonic quantum processors could largely reduce their currently prohibitive footprint. The performance of such hybrid platforms will rely, among others, on the ability to coherently engineer and control spin-wave pulses in the classical regime—a capability proven by this work—and in the quantum regime. Future extensions of our work include exploring coherent propagation of quantum magnonic states and their control using external quantum systems, e.g., solid-state emitters [16].

ACKNOWLEDGMENTS

We acknowledge discussions with O. Dobrovolskiy, J.J. García Ripoll, and T. Agrenius. The computational results presented here have been achieved (in part) using the LEO HPC infrastructure of the University of Innsbruck. This work is supported by the Austrian Science Fund (FWF) through Project No. I 4917-N (MagFunc). S.K. acknowledges the support by the H2020-MSCA-IF under the Grant No. 101025758 (OMNI).

APPENDIX A: WAVEGUIDE AND ANTENNA CHARACTERIZATION

We determine the waveguide static magnetization and dispersion relation using MuMax3 [26]. To compute the dispersion relation we evolve the magnetization under a magnetic field $\mathbf{B}_1(\mathbf{r}, t) \propto \mathbf{B}_a(\mathbf{r}) \sin(\omega_{\max} t)/t$, able to excite spin waves in a wide range of frequencies ($\omega < \omega_{\max}$) and wave vectors. Applying a two-dimensional Fourier transform to the simulated magnetization leads to the excitation spectrum of the spin waves,

$$\mathbf{m}(k, 0, 0, \omega) = \frac{1}{2\pi} \int_{\mathbb{R}} \int_{\mathbb{R}} dx\, dt\, \mathbf{m}(x, 0, 0, t) e^{-i(kx+\omega t)}. \tag{A1}$$

Two examples of these spectra for different waveguides and $\omega_{\max}/(2\pi) = 10$ GHz are shown in Fig. 1(b). The spin-wave frequency for each wave number k can then be extracted as the maximum of the excitation spectrum for such a wave number (red dashed curves in the figure).

We model the field generated by the antenna at the waveguide by the Gaussian function

$$\mathbf{B}_a(\mathbf{r}) = \frac{|\mathbf{B}_0| L_z}{\sqrt{2\pi}\sigma_a} \exp\left(-\frac{x^2}{2\sigma_a^2}\right) \mathbf{e}_z, \tag{A2}$$

where L_z is the width of the waveguide along the z direction and $\mathbf{B}_0$ is the homogeneous bias field [note that the driving strength is encoded in the function $V(t)$]. The physical width of the antenna can be identified with the full width at half maximum of the field profile, $w_a = 2\sqrt{2\log(2)}\sigma_a \approx 2.3\sigma_a$. To determine the antenna transfer function, we first define the Fourier transform for a vector function as $\mathbf{v}(t)$ as $\mathcal{F}\{\mathbf{v}(t)\} \equiv (\sqrt{2\pi})^{-1} \int_{\mathbb{R}} dt \mathbf{v}(t) \exp(-i\omega t)$. Then, for every chosen antenna (i.e., for every value of σ_a) we perform one micromagnetic simulation of the magnetization dynamics in the presence of the driving field Eq. (A2), using an impulse test driving $V_{\text{test}}(t) = \delta(t)$. For this driving, the transfer function in time domain is simply proportional to the magnetization field, $\mathbf{f}(\mathbf{r}, t) = \sqrt{2\pi}\,\mathbf{m}(\mathbf{r}, t)$. To determine the transfer function in Fig. 1(c) (left panel) we use an impulse driving $V(t) = 0.15$ during a single time step of 1 ps and $V(t) = 0$ afterward. The antenna field width is chosen as $\sigma_a = 30$ nm, corresponding to an antenna width of about $w_a \approx 70$ nm. In Fig. 1(c) (right panel) we choose $\sigma_a = 100$ nm, corresponding to $w_a \approx 230$ nm, and an amplitude of the impulse driving $V(t) = 0.4$ during a single time step of 1 ps.

In Figs. 2 and 3 we model the system as a finite waveguide of dimensions (80 μm × 50 nm × 50 nm), with material parameters for YIG [24], namely saturation magnetization $M_s = 140.7$ kA m^{-1}, exchange constant $A_{\text{ex}} = 4.2$ pJ m^{-1}, Gilbert damping parameter $\alpha = 1.75 \times 10^{-4}$, and a cell size of $(10 \times 6.25 \times 6.25)$ nm^3. For Fig. 4 we use a waveguide of dimensions (80 μm × 200 nm × 100 nm) with the same material parameters described above, and a cell size of $(10 \times 10 \times 10)$ nm^3. In both cases we assume free-pinning boundary conditions at all the surfaces and neglect magnetocrystalline anisotropy. These assumptions are known to accurately reproduce experimental measurements of spin-wave dispersion and dynamics in the chosen nanowaveguides [9,24].

APPENDIX B: BACKWARD PROPAGATION OF THE PULSE

In order to perform the backward propagation in a fast way, we obtain an analytical approximation for the dispersion relation $\omega(k)$ by fitting the maxima of the magnetization spectrum to a sixth-order polynomial in k. The resulting polynomial approximations, shown in (b) of Figs. 2–4, are then used to integrate Eq. (1) numerically. The maximum error incurred by this polynomial approximation is below 0.25% for all the wave numbers in Figs. 2

and 3 and below 0.45% in Fig. 4. The integral is computed back to a time $t = 0$ defined as the time at which 99.5% of the pulse lies at the opposite side of the antenna, i.e.,

$$\left|\frac{\int_{L_0}^{x_a} dx(\mathbf{e}_0 \cdot \mathbf{m}_T(x, y_0, z_0, 0))^2}{\int_{\mathbb{R}} dx(\mathbf{e}_0 \cdot \mathbf{m}_T(x, y_0, z_0, 0))^2}\right| = 0.995, \tag{B1}$$

where $L_0 \equiv -\infty$ ($L_0 \equiv +\infty$) for rightward (left)-propagating pulses.

APPENDIX C: DEFINITION OF PULSE WIDTH, PULSE DURATION, AND MINIMUM WAVELENGTH

We define the time-dependent width of a given pulse as the standard deviation of the pulse position, i.e.,

$$\sigma(t) \equiv \sqrt{\int_{\mathbb{R}} dx \frac{(\mathbf{e_0} \cdot \mathbf{m}(x, y_0, z_0, t))^2}{N^2(t)} (x - \bar{x}(t))^2}, \tag{C1}$$

where $N^2(t) \equiv \int_{\mathbb{R}} dx(\mathbf{e}_0 \cdot \mathbf{m}(x, y_0, z_0, t))^2$ is a normalization factor and $\bar{x}(t) \equiv \int_{\mathbb{R}} dx\, x\, (\mathbf{e}_0 \cdot \mathbf{m}(x, y_0, z_0, t))^2/N^2(t)$ is the mean value of the pulse position.

The position-dependent pulse duration is defined as

$$\sigma_t(x) \equiv \sqrt{\int_{\mathbb{R}} dt \frac{(\mathbf{e_0} \cdot \mathbf{m}(x, y_0, z_0, t))^2}{N_t^2(x)} (t - \bar{t}(x))^2}, \tag{C2}$$

where $N_t^2(x) \equiv \int_{\mathbb{R}} dt(\mathbf{e}_0 \cdot \mathbf{m}(x, y_0, z_0, t))^2$ is a normalization factor and $\bar{t}(x) \equiv \int_{\mathbb{R}} dt\, t\, (\mathbf{e}_0 \cdot \mathbf{m}(x, y_0, z_0, t))^2/N^2(t)$.

The minimum wavelength of each pulse is defined as $\lambda_{\min} \equiv 2\pi/k_{\max}$, where we define $k_{\max}$ such that

$$\frac{\int_{-\infty}^{k_{\max}} dk|\mathcal{F}^{-1}\{m_T(x)\}|}{\int_{-\infty}^{\infty} dk|\mathcal{F}^{-1}\{m_T(x)\}|} = 0.997. \tag{C3}$$

Here $m_T(k) \equiv (\sqrt{2\pi})^{-1} \int_{\mathbb{R}} dt m_T(x) \exp(ikx)$ is the inverse Fourier transform of the target pulse $m_T(x)$ in position space. For the Gaussian pulse Eq. (2), the condition Eq. (C3) corresponds to $k_{\max} = k_0 + 2/\sigma_f$.

APPENDIX D: ENERGY COST OF GENERATING THE DRIVING FIELD

The energy required to generate a pulse is lower bounded by the total energy required to generate the driving field. We define the following figure of merit for the latter:

$$U_{\max} \equiv \max_t \int_V d^3\mathbf{r} \int_{-\infty}^{t} dt' \mathbf{H}_1(\mathbf{r}, t') \cdot \frac{\partial}{\partial t'} \mathbf{B}_1(\mathbf{r}, t'), \tag{D1}$$

where V denotes the volume of the waveguide. Equation (D1) corresponds to the maximum value of the instantaneous magnetic energy held inside the waveguide due to the presence of a driving field $\mathbf{B}_1(\mathbf{r}, t)$ [52]. Both fields in the integrand of Eq. (D1) are assumed to vanish at $t' = -\infty$ and are related in frequency domain by

$$\mathbf{H}_1(\mathbf{r}, \omega) = \frac{1}{\mu_0} \bar{\boldsymbol{\mu}}^{-1}(\omega) \mathbf{B}_1(\mathbf{r}, \omega), \tag{D2}$$

where μ_0 is the vacuum permeability and $\bar{\boldsymbol{\mu}}(\omega)$ is the relative permeability tensor.

In frequency domain, all pulses considered in this paper have central frequencies near $\omega_0 \equiv |\gamma \mathbf{B}_0|$, where $\mathbf{B}_0$ is the homogeneous bias field and γ is the gyromagnetic ratio, and widths much smaller than ω_0. We can thus approximate $\bar{\boldsymbol{\mu}}^{-1}(\omega) \approx \bar{\boldsymbol{\mu}}^{-1}(\omega_0)$ in the above expression. Using the identity $\mathbf{B}_1(\mathbf{r}, t) = \mathbf{B}_a(\mathbf{r}) V(t)$ and assuming that the only nonzero component of $\mathbf{B}_a(\mathbf{r})$ is oriented along the unit vector $\mathbf{e}_z$, we cast the energy as

$$U_{\max} = \frac{L_y L_z}{2\mu_0} \left[\bar{\boldsymbol{\mu}}^{-1}(\omega_0)\right]_{zz} \int_{\mathbb{R}} dx\, |\mathbf{B}_a(\mathbf{r})|^2 \max_t V^2(t). \tag{D3}$$

The energy $U_{\max}$ as a function of the antenna width is displayed in Fig. 5(b). It is normalized to a reference energy U_0, namely the energy stored by the constant homogeneous bias field $\mathbf{B}_0$ in a section of the waveguide large enough to contain the pulse at all times, given by $U_0 = L_x L_y L_z |\mathbf{B}_0|^2/(2\mu_0)$ with $L_z = 80$ μm taken as the length of our micromagnetic simulation domain. In particular, $U_0 = 5.83$ fJ for the homogeneous field used in the generation of pulses in the exchange regime and $U_0 = 1.59$ fJ for the dipolar pulse. To compute the value of $U_{\max}$, we approximate the inverse permeability tensor by its Polder susceptibility expression [52],

$$\left[\bar{\boldsymbol{\mu}}^{-1}(\omega_0)\right]_{zz} \approx \frac{1}{2 + (\mu_0 M_s/|\mathbf{B}_0|)}, \tag{D4}$$

where M_s is the saturation magnetization of the waveguide.

[1] A. Barman, G. Gubbiotti, S. Ladak, A. O. Adeyeye, M. Krawczyk, J. Gräfe, C. Adelmann, S. Cotofana, A. Naeemi, V. I. Vasyuchka, and B. Hillebrands, The 2021 magnonics roadmap, J. Phys.: Condens. Matter **33**, 413001 (2021).

[2] A. V. Chumak, P. Kabos, M. Wu, C. Abert, C. Adelmann, A. O. Adeyeye, J. Åkerman, F. G. Aliev, A. Anane, A. Awad, and C. H. Back, Advances in magnetics roadmap on spin-wave computing, IEEE Trans. Magn. **58**, 1 (2022).

[3] D. Lachance-Quirion, Y. Tabuchi, A. Gloppe, K. Usami, and Y. Nakamura, Hybrid quantum systems based on magnonics, Appl. Phys. Express **12**, 070101 (2019).

[4] A. V. Chumak, V. I. Vasyuchka, A. A. Serga, and B. Hillebrands, Magnon spintronics, Nat. Phys. **11**, 453 (2015).

[5] P. Pirro, V. I. Vasyuchka, A. A. Serga, and B. Hillebrands, Advances in coherent magnonics, Nat. Rev. Mater. **6**, 1114 (2021).

[6] B. Rana and Y. Otani, Towards magnonic devices based on voltage-controlled magnetic anisotropy, Commun. Phys. **2**, 90 (2019).

[7] J. Chen, H. Yu, and G. Gubbiotti, Unidirectional spin-wave propagation and devices, J. Phys. D: Appl. Phys **55**, 123001 (2021).

[8] H. Yu, J. Xiao, and H. Schultheiss, Magnetic texture based magnonics, Phys. Rep. **905**, 1 (2021).

[9] B. Heinz, T. Brächer, M. Schneider, Q. Wang, B. Lägel, A. M. Friedel, D. Breitbach, S. Steinert, T. Meyer, M. Kewenig, C. Dubs, P. Pirro, and A. V. Chumak, Propagation of spin-wave packets in individual nanosized yttrium iron garnet magnonic conduits, Nano Lett. **20**, 4220 (2020).

[10] B. Divinskiy, H. Merbouche, K. Nikolaev, S. Michaelis de Vasconcellos, R. Bratschitsch, D. Gouéré, R. Lebrun, V. Cros, J. Ben Youssef, P. Bortolotti, A. Anane, S. Demokritov, and V. Demidov, Dispersionless Propagation of Ultrashort Spin-Wave Pulses in Ultrathin Yttrium Iron Garnet Waveguides, Phys. Rev. Appl. **16**, 024028 (2021).

[11] E. Albisetti, D. Petti, G. Sala, R. Silvani, S. Tacchi, S. Finizio, S. Wintz, A. Calò, X. Zheng, J. Raabe, E. Riedo, and R. Bertacco, Nanoscale spin-wave circuits based on engineered reconfigurable spin-textures, Commun. Phys **1**, 56 (2018).

[12] G. Talmelli, T. Devolder, N. Träger, J. Förster, S. Wintz, M. Weigand, H. Stoll, M. Heyns, G. Schütz, I. P. Radu, J. Gräfe, F. Ciubotaru, and C. Adelmann, Reconfigurable submicrometer spin-wave majority gate with electrical transducers, Sci. Adv. **6**, eabb4042 (2020).

[13] Q. Wang, M. Kewenig, M. Schneider, R. Verba, F. Kohl, B. Heinz, M. Geilen, M. Mohseni, B. Lägel, F. Ciubotaru, C. Adelmann, C. Dubs, S. D. Cotofana, O. V. Dobrovolskiy, T. Brächer, P. Pirro, and A. V. Chumak, A magnonic directional coupler for integrated magnonic half-adders, Nat. Electron. **3**, 765 (2020).

[14] M. Vogel, A. V. Chumak, E. H. Waller, T. Langner, V. I. Vasyuchka, B. Hillebrands, and G. von Freymann, Optically reconfigurable magnetic materials, Nat. Phys. **11**, 487 (2015).

[15] Q. Wang, A. V. Chumak, and P. Pirro, Inverse-design magnonic devices, Nat. Commun. **12**, 2636 (2021).

[16] C. Gonzalez-Ballestero, T. van der Sar, and O. Romero-Isart, Towards a quantum interface between spin waves and paramagnetic spin baths, Phys. Rev. B **105**, 075410 (2022).

[17] M. Fukami, D. R. Candido, D. D. Awschalom, and M. E. Flatté, Opportunities for Long-Range Magnon-Mediated Entanglement of Spin Qubits via On- and Off-Resonant Coupling, PRX Quantum **2**, 040314 (2021).

[18] I. Bertelli, J. J. Carmiggelt, T. Yu, B. G. Simon, C. C. Pothoven, G. E. W. Bauer, Y. M. Blanter, J. Aarts, and T. van der Sar, Magnetic resonance imaging of spin-wave transport and interference in a magnetic insulator, Sci. Adv. **6**, eabd3556 (2020).

[19] B. G. Simon, S. Kurdi, H. La, I. Bertelli, J. J. Carmiggelt, M. Ruf, N. de Jong, H. van den Berg, A. J. Katan, and T. van der Sar, Directional excitation of a high-density magnon gas using coherently driven spin waves, Nano Lett. **21**, 8213 (2021).

[20] R. G. Kryshtal and A. V. Medved, Nonlinear spin waves in dynamic magnonic crystals created by surface acoustic waves in yttrium iron garnet films, J. Phys. D: Appl. Phys **50**, 495004 (2017).

[21] A. V. Chumak, P. Dhagat, A. Jander, A. A. Serga, and B. Hillebrands, Reverse Doppler effect of magnons with negative group velocity scattered from a moving Bragg grating, Phys. Rev. B **81**, 140404 (2010).

[22] Á. Papp, W. Porod, and G. Csaba, Nanoscale neural network using non-linear spin-wave interference, Nat. Commun. **12**, 6422 (2021).

[23] M. Kiechle, L. Maucha, V. Ahrens, C. Dubs, W. Porod, G. Csaba, M. Becherer, and A. Papp, Experimental demonstration of a spin-wave lens designed with machine learning, IEEE Magn. Lett. **13**, 1 (2022).

[24] B. Heinz, Q. Wang, M. Schneider, E. Weiss, A. Lentfert, B. Lägel, T. Brächer, C. Dubs, O. V. Dobrovolskiy, P. Pirro, and A. V. Chumak, Long-range spin-wave propagation in transversely magnetized nano-scaled conduits, Appl. Phys. Lett. **118**, 132406 (2021).

[25] B. Heinz, M. Mohseni, A. Lentfert, R. Verba, M. Schneider, B. Lägel, K. Levchenko, T. Brächer, C. Dubs, A. V. Chumak, and P. Pirro, Parametric generation of spin waves in nano-scaled magnonic conduits, (2021), arXiv preprint ArXiv:2106.10727.

[26] A. Vansteenkiste, J. Leliaert, M. Dvornik, M. Helsen, F. Garcia-Sanchez, and B. Van Waeyenberge, The design and verification of MuMax3, AIP Adv. **4**, 107133 (2014).

[27] Y.-J. Lu, R. Sokhoyan, W.-H. Cheng, G. Kafaie Shirmanesh, A. R. Davoyan, R. A. Pala, K. Thyagarajan, and H. A. Atwater, Dynamically controlled Purcell enhancement of visible spontaneous emission in a gated plasmonic heterostructure, Nat. Commun. **8**, 1631 (2017).

[28] K. F. MacDonald, Z. L. Sámson, M. I. Stockman, and N. I. Zheludev, Ultrafast active plasmonics, Nat. Photon. **3**, 55 (2009).

[29] C. F. Roos, Ion trap quantum gates with amplitude-modulated laser beams, New J. Phys. **10**, 013002 (2008).

[30] C. Li, V. Gusev, T. Dekorsy, and M. Hettich, All optical control of comb-like coherent acoustic phonons in multiple quantum well structures through double-pump-pulse pump-probe experiments, Opt. Express **27**, 18706 (2019).

[31] A. Sharafiev, M. L. Juan, O. Gargiulo, M. Zanner, S. Wögerer, J. J. García-Ripoll, and G. Kirchmair, Visualizing the emission of a single photon with frequency and time resolved spectroscopy, Quantum **5**, 474 (2021).

[32] S.-L. Zhu, C. Monroe, and L.-M. Duan, Trapped Ion Quantum Computation with Transverse Phonon Modes, Phys. Rev. Lett. **97**, 050505 (2006).

[33] G. Zarantonello, H. Hahn, J. Morgner, M. Schulte, A. Bautista-Salvador, R. F. Werner, K. Hammerer, and C. Ospelkaus, Robust and Resource-Efficient Microwave Near-Field Entangling $^9\mathrm{Be}^+$ Gate, Phys. Rev. Lett. **123**, 260503 (2019).

[34] J. O'Sullivan, O. W. Kennedy, K. Debnath, J. Alexander, C. W. Zollitsch, M. Šimėnas, A. Hashim, C. N. Thomas, S. Withington, I. Siddiqi, K. Mølmer, and J. J. L. Morton, Random-Access Quantum Memory Using Chirped Pulse Phase Encoding, Phys. Rev. X **12**, 041014 (2022).

[35] M. Khanahmadi and K. Mølmer, Qubit readout and quantum sensing with pulses of quantum radiation, Phys. Rev. A **107**, 013705 (2023).

[36] F. Ciubotaru, T. Devolder, M. Manfrini, C. Adelmann, and I. P. Radu, All electrical propagating spin wave spectroscopy with broadband wavevector capability, Appl. Phys. Lett. **109**, 012403 (2016).

[37] M. Vaňatka, K. Szulc, O. c. v. Wojewoda, C. Dubs, A. V. Chumak, M. Krawczyk, O. V. Dobrovolskiy, J. W. Kłos, and M. Urbánek, Spin-Wave Dispersion Measurement by Variable-Gap Propagating Spin-Wave Spectroscopy, Phys. Rev. Appl. **16**, 054033 (2021).

[38] S. Knauer, K. Davídková, D. Schmoll, R. O. Serha, A. Voronov, Q. Wang, R. Verba, O. V. Dobrovolskiy, M. Lindner, T. Reimann, C. Dubs, M. Urbánek, and A. V. Chumak, Propagating spin-wave spectroscopy in nanometer-thick YIG films at millikelvin temperatures, J. Appl. Phys. to be published.

[39] In general, the generated magnetization in frequency domain is proportional to both the applied voltage $V_{\mathrm{ac}}(\omega)$ and the voltage-to-spin-wave transmission efficiency of the antenna $t(\omega)$. The latter is strongly dependent on the particular configuration and can be determined via, e.g., finite-element simulations or from spin-wave transmission measurements. Hereafter we assume $t(\omega) = 1$. For $t(\omega) \neq 1$, the voltage signal can be directly computed from our method as $V_{\mathrm{ac}}(\omega) = V(\omega)/t(\omega)$.

[40] S. Casulleras, C. Gonzalez-Ballestero, P. Maurer, J. J. García-Ripoll, and O. Romero-Isart, Remote Individual Addressing of Quantum Emitters with Chirped Pulses, Phys. Rev. Lett. **126**, 103602 (2021).

[41] M. Bauer, O. Büttner, S. O. Demokritov, B. Hillebrands, V. Grimalsky, Y. Rapoport, and A. N. Slavin, Observation of Spatiotemporal Self-Focusing of Spin Waves in Magnetic Films, Phys. Rev. Lett. **81**, 3769 (1998).

[42] A. A. Serga, S. O. Demokritov, B. Hillebrands, and A. N. Slavin, Self-Generation of Two-Dimensional Spin-Wave Bullets, Phys. Rev. Lett. **92**, 117203 (2004).

[43] A. A. Serga, B. Hillebrands, S. O. Demokritov, A. N. Slavin, P. Wierzbicki, V. Vasyuchka, O. Dzyapko, and A. Chumak, Parametric Generation of Forward and Phase-Conjugated Spin-Wave Bullets in Magnetic Films, Phys. Rev. Lett. **94**, 167202 (2005).

[44] O. R. Sulymenko, O. V. Prokopenko, V. S. Tyberkevych, A. N. Slavin, and A. A. Serga, Bullets and droplets: Two-dimensional spin-wave solitons in modern magnonics (review article), Low Temp. Phys. **44**, 602 (2018).

[45] A. Hamadeh, D. Breitbach, M. Ender, A. Koujok, M. Mohseni, F. Kohl, J. Maskill, M. Bechberger, and P. Pirro, Hybrid magnonic-oscillator system, J. Appl. Phys. **132**, 183904 (2022).

[46] T. Brächer and P. Pirro, An analog magnon adder for all-magnonic neurons, J. Appl. Phys. **124**, 152119 (2018).

[47] R. Albert, E. I. Zanner, M. Rosenthal, S. Casulleras, M. Juan, K. Lehnert, O. Romero-Isart, and G. Kirchmair, to be published.

[48] Á. Papp, W. Porod, and G. Csaba, Nanoscale neural network using non-linear spin-wave interference, Nat. Commun. **12**, 1 (2021).

[49] A. Mahmoud, F. Ciubotaru, F. Vanderveken, A. V. Chumak, S. Hamdioui, C. Adelmann, and S. Cotofana, Introduction to spin wave computing, J. Appl. Phys. **128**, 161101 (2020).

[50] J. J. Carmiggelt, O. C. Dreijer, C. Dubs, O. Surzhenko, and T. van der Sar, Electrical spectroscopy of the spin-wave dispersion and bistability in gallium-doped yttrium iron garnet, Appl. Phys. Lett. **119**, 202403 (2021).

[51] T. Böttcher, M. Ruhwedel, K. O. Levchenko, Q. Wang, H. L. Chumak, M. A. Popov, I. V. Zavislyak, C. Dubs, O. Surzhenko, B. Hillebrands, A. V. Chumak, and P. Pirro, Fast long-wavelength exchange spin waves in partially compensated Ga:YIG, Appl. Phys. Lett. **120**, 102401 (2022).

[52] D. Stancil and A. Prabhakar, *Spin Waves: Theory and Applications* (Springer, US, 2009).